Structural Dynamics and Attitude Control of a Solar Sail Using Tip Vanes

Mirue Choi* and Christopher J. Damaren†
University of Toronto, Toronto, Ontario M3H 5T6, Canada

DOI: 10.2514/1.A33179

This paper delves into the structural and attitude dynamics of a cord-mat square solar sail being controlled by two-degree-of-freedom tip-vane actuation. The paper's main goal is to simulate and analyze the behavior of a solar sail under a tip-vane attitude control scheme using a geometrically nonlinear elastic finite element method model of the sail. The controller/structural interaction is of particular interest, as the control solution of the two-degree-of-freedom tip-vane actuation is based on a flat, inflexible sail. The sail structure is further augmented by a wrinkling model for handling the membranes under negative strain. The model is further augmented by the disturbance forces produced by the reflective sail membrane itself. A combined, dynamic simulation of all of the aforementioned are performed to analyze the performance of the control system as a whole.

Nomenclature

A	=	area of the reflected surface
a, b	=	material state parameters for the stress–strain constitutive relationship
$\hat{a}, \varphi$	=	coefficients of axis-angle representation
C_{ij}	=	rotation matrix from frame i to frame j
$C_{i,\alpha}$	=	principal rotation of angle α about i axis
D	=	damping matrix
E	=	Young's modulus
E	=	stress–strain constitutive relationship matrix
$\mathcal{F}$	=	coordinate frame
f	=	forcing column matrix
f_α	=	generalized elastic stiffness force associated with shape function of element α
$\boldsymbol{f}$	=	forcing vector
f_{ideal}	=	ideal solar radiation pressure force
G_i	=	torque along i axis
$\hat{G}$	=	normalized solar radiation pressure torque
h	=	membrane thickness
I	=	area moment of inertia of beam cross section
K	=	stiffness matrix
K_d	=	derivative control gain matrix
k_p	=	proportional control gain
L	=	distance between two ends of the support cord, m
L_s	=	distance between edge of one support cord to the next, m
M	=	mass matrix
$[M]^\times$	=	cross-product operator
m, k	=	damping parameters
n_i	=	vane i normal vector component
$\hat{\boldsymbol{n}}$	=	unit normal vector for reflective surface
P	=	pressure exerted on the surface by the solar radiation pressure
p	=	vertex
$\tilde{p}_i$	=	point i of convex hull set
q	=	composite state variables
q_e	=	column matrix of the elastic generalized coordinates
q_n	=	components of quaternion
R, Q	=	parameters of wrinkled membrane stress–strain constitutive relationship matrix
$\boldsymbol{R}$	=	absolute position vector
S_α, C_α	=	sine and cosine of angle α
$\hat{\boldsymbol{s}}$	=	unit vector from the sun to a point on the surface
u_i	=	deformation of node i of the triangular element in body frame
u_j	=	first derivative of x-axis deformation function with regard to j
u_{jk}	=	second derivative of x-axis deformation function with regard to j and k
$\boldsymbol{u}$	=	deformation of unit mass
V	=	volume
v	=	components of the absolute velocity vector
v_i	=	location of node i of the triangular element in body frame
α, β	=	cone and clock angle of sun vector
Γ	=	ratio between inward camber and distance between two ends of the support cord
γ_{ij}	=	shear strain function with regard to i and j
Δ	=	ratio between depth and distance between one end of support cord to other
δ	=	infinitesimal positive number
$\boldsymbol{\epsilon}$	=	vector component of quaternion
ϵ	=	strain
η	=	scalar component of quaternion
θ_i	=	desired orientation in Euler angles about i axis
ν	=	Poisson's ratio
$\boldsymbol{\xi}$	=	rigid state variables
ρ	=	density
$\boldsymbol{\rho}_i$	=	original location of node i of the triangular element in body frame
$\boldsymbol{\rho}$	=	body frame displacement of unit mass
ς_1, ς_2	=	parameters for material state criteria determination
τ	=	stress
ϕ_i, θ_i	=	vane rotations
$\boldsymbol{\chi}$	=	control input
$\boldsymbol{\psi}_\alpha$	=	shape function of element α
Ω	=	ratio between depth and distance between edge of one support cord to the next
$\boldsymbol{\omega}$	=	components of the angular velocity vector
1_3	=	3×3 identity matrix

Presented as Paper 2015-0433 at the 2nd AIAA Spacecraft Structures Conference, AIAA Science and Technology Forum 2015, Gaylord Palms Convention Center, Kissimmee, FL, 5–9 January 2015; received 9 October 2014; revision received 1 February 2015; accepted for publication 17 April 2015; published online 1 October 2015.

*Institute for Aerospace Studies, 4925 Dufferin Street; currently Operations Engineer, BlackBridge, Kurfürstendamm 22, Berlin, Germany.

†Professor, Institute for Aerospace Studies, 4925 Dufferin Street. Associate Fellow AIAA.

I. Introduction

THE concept of solar sailing, which is a propulsion method that harnesses the momentum carried by the light photons via large reflective surfaces, has waxed and waned in its popularity over

the century. With the success of the Japan Aerospace Exploration Agency's Interplanetary Kitecraft Accelerated by Radiation of the Sun (IKAROS) experimental sailcraft in the recent years, the interest in solar sailing has once again waxed, prompting renewed work. In particular, NASA's Sunjammer project is of great interest, with its traditional square sail setup with boom deployment and vane-based attitude control scheme.

This paper focuses on a design of a solar sail similar to that of the Sunjammer, with the key goal of simulating its dynamical behavior and applying a vane control scheme designed by the authors to this dynamic model. Considerations such as overall mass, membrane packing, and sail deployability drive the sail to be very thin and flexible. Since the sail's capability to produce thrust is directly affected by the shape of the reflective surface, the structural dynamics and the associated changes in the sail thrust are of great interest. Also, with the goal of applying a vane control scheme designed for attitude control, the sail's rotational dynamics are of interest. In this research, combined rigid and structural dynamics equations of motions are used to simulate the sail's dynamic behavior in space, accounting for the effect of rigid dynamics on the elastic dynamics and vice versa. A method for estimating the forces produced by the sail shape predicted by the dynamics model is used to predict its effect on the sail's attitude as the simulation progresses.

In addition to the aforementioned, other considerations unique to a solar sail are explored as well. One such consideration is the sail wrinkling: simulating the dynamics of a membrane is not an easy endeavor due to its tendency to behave nonelastically by wrinkling and slacking. Simulating the behavior of wrinkling membranes is an active area of research, and numerous papers with methods of handling this problem are available. One such method, modified to handle slacking cases as well, is presented in this paper and used in the simulation.

The second consideration is the effect of shadowing on the sail. Certain pathological orientations and placement of other components of the spacecraft may cast a shadow upon the sail, which then no longer produces thrust as long as the shadow remains. Predicting where and how such shadowing occurs adds another level of fidelity to the simulation. In this paper, a method of determining the shadowed region on the sail surface is presented, using the method to show how a spacecraft bus and the sail surface can cast shadow upon the sail at certain orientations.

Apart from the aforementioned, the vane control scheme designed by the authors is briefly introduced; then, it is combined with a generic proportional-derivative (PD) control law to provide attitude control over the sail. The dynamics model with all the augmentations from the preceding are combined with this control law using angular velocity and quaternion (Euler parameter) feedback to show its capability with a number of attitude pointing maneuver simulations. Special attention is given to the sail behavior, the produced control, and disturbance torques, as well as the performance of the controller in terms of the settling time and the severity of the vane angle changes.

Our major contribution is to explore the potential for control-structure interaction when tip vanes are used to implement the control torques. In this case, the noncollocation of the applied control influences and the sensed variables (the angular velocity and sail attitude) raises the possibility of destabilization of the control law. We note that previous studies of the attitude control of solar sails [1–5] have employed rigid sail models, and hence could not address this point. Furthermore, we employ two-degree-of-freedom tip vanes, whereas previous studies have employed single-degree-of-freedom tip vanes (which do not render the sail fully controllable and need to be augmented by other actuation).

II. Cord-Mat Solar Sail Model

A common design found in the literature is that of a square solar sail, where the thin reflective membranes are stretched between four equal-length support booms [1–14]. Here, a variant design of the square sail is used: a cord-mat solar sail model, introduced by Greschik [8] and illustrated in Fig. 1. This design is notable in that it inherently does not stretch the sail membrane but, instead, it is "spread onto" (and attached to) a set of cords suspended between the support booms. Due to the nature of the design, some billowing occurs with the sail, but the shape and the size of the billow would be controlled by the cords. Any loading onto the support boom is restricted to that from the cords, allowing for more predictable loading on the booms. However, the membrane slackness has an inherent downside to it, which is that it makes the prediction of the sail membrane dynamics and the resulting solar radiation pressure (SRP) force a complicated matter.

It is assumed that the suspension cords, under a slack, stable initial state with very small uniform lateral external loading, form a catenary sag in the direction of the loading. A quadrant of the sail in such an initial state is shown in Fig. 1b. The key preconstructed sags in the sail surface geometries are noted in this figure.

These sags are described as follows: first, the support cords are sagged in the out-of-plane direction in a gradually deepening set of catenaries, such that, at the edge of the quadrant, the depth of the sag is described by a unitless quantity Δ, which is the ratio between the actual depth and the distance between the one end of the cord to the other. The catenary itself is described by the following equation:

$$y = \frac{\Delta}{L}x^2 - L\Delta \tag{1}$$

where L is the distance between the two ends of the cord, x is any point along this distance, and y is the depth. It is assumed that, at one end of the cord, $x = y = 0$ and, at the other end of the cord, $x = L$ and $y = 0$.

The other two sags are described in a similar fashion as before. An inward sag is imposed upon the outer sail edge, noted by the unitless parameter Γ in the diagram: a ratio between the actual inward camber and L. This, noted by Greschik in his paper [8], is due to a small amount of inward tension applied to the cord due to the membrane. Although this camber can be spread out among the outer cords, for simplicity, it is assumed that the inward camber exists only for the outermost cords.

Lastly, the sail membrane in between the cords is assumed to be slack; hence, a catenary is formed here as well. It is worth noting that the depth of this film billow is measured from the cord, which is also curved. Hence, the resulting portion of sail membrane forms a curvature, with its shape defined by Ω and Δ (and Γ as well in the case

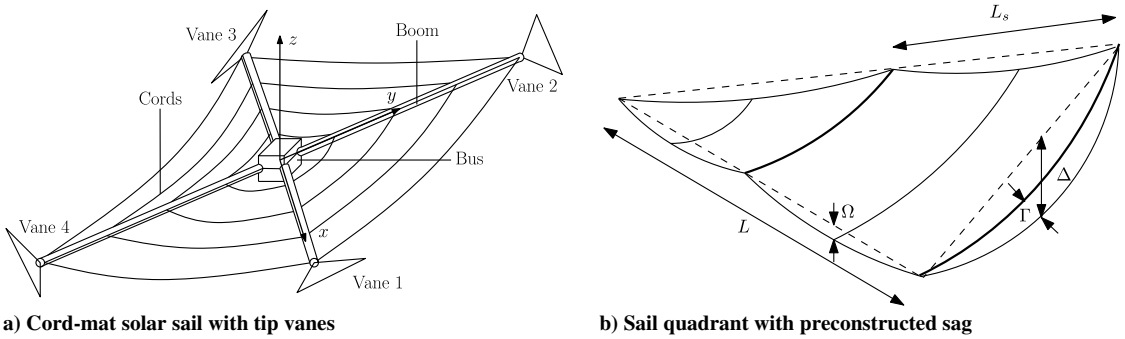

a) Cord-mat solar sail with tip vanes **b) Sail quadrant with preconstructed sag**

Fig. 1 Cord-mat solar sail.

of the outermost portion of the membrane). Here, Ω is a ratio between the actual depth and the distance between the edge of one cord to the next L_s.

III. Unconstrained Nonlinear Dynamics of the Sail

To analyze the effect of the flexible sail on its attitude dynamics, a geometrically nonlinear finite element method (FEM) model and its simulation system are developed. Only the generalized equations of motion and the FEM model are described here, with the derivation and implementation details of the equations, the model, and the simulator omitted due to their complexity. These details are available in Choi's thesis [15] for perusal.

The dynamics of a flexible object, such as the one given in Fig. 2, are derived from the absolute position vector $\boldsymbol{R}$; Newton's second law of motion

$$\iiint_V \boldsymbol{f}_e \, \mathrm{d}m = \iiint_V \ddot{\boldsymbol{R}} \, \mathrm{d}m \tag{2}$$

and its cross-multiplied variant

$$\iiint_V (\boldsymbol{\rho} + \boldsymbol{u}) \times \ddot{\boldsymbol{R}} \, \mathrm{d}m = \iiint_V (\boldsymbol{\rho} + \boldsymbol{u}) \times \boldsymbol{f}_e \, \mathrm{d}m \tag{3}$$

where $\boldsymbol{\rho}$ and $\boldsymbol{u}$ are the body frame displacement and the deformation of a mass dm; and the equilibrium of the generalized elastic forces

$$\iiint_V \boldsymbol{\psi}_\alpha^T \boldsymbol{f}_e \, \mathrm{d}m = \iiint_V \boldsymbol{\psi}_\alpha^T \ddot{\boldsymbol{R}} \, \mathrm{d}m + f_\alpha, \qquad \alpha = 1, 2, 3, \ldots \tag{4}$$

where $\boldsymbol{\psi}_\alpha$ is a shape function, f_e is the external forcing, and f_α refers to the generalized elastic stiffness force associated with the shape function ψ_α. After a lengthy derivation process that does not assume small deformations, one can combine, expand, and rewrite the preceding expressions as the following equations of motion:

$$\begin{bmatrix} M_{rr}(q_e) & M_{re}(q_e) \\ M_{re}^T(q_e) & M_{ee} \end{bmatrix} \begin{bmatrix} \dot{\boldsymbol{\xi}} \\ \ddot{q}_e \end{bmatrix} + \begin{bmatrix} \boldsymbol{0} & \boldsymbol{0} \\ \boldsymbol{0} & K_{ee}(q_e) \end{bmatrix} \times \begin{bmatrix} \gamma \\ q_e \end{bmatrix} = \begin{bmatrix} f_{T,r}(q, \boldsymbol{\chi}) \\ f_{T,e}(\boldsymbol{\chi}) \end{bmatrix} + \begin{bmatrix} f_{I,r}(q) \\ f_{I,e}(q) \end{bmatrix} \tag{5}$$

or

$$M(q)\ddot{q} + K(q)q = f_T(q, \boldsymbol{\chi}) + f_I(q, \dot{q}) \tag{6}$$

where the state variables $\boldsymbol{\xi} = [\, v^T \quad \boldsymbol{\omega}^T \,]^T$, $\dot{q} = [\, \boldsymbol{\xi}^T \quad \dot{q}_e^T \,]^T$, $q = [\, \boldsymbol{\gamma}^T \quad q_e^T \,]^T$, v, and $\boldsymbol{\omega}$ are the components of the absolute velocity vector and the angular velocity vector of the body frame $\mathcal{F}_b$ with respect to the inertial frame $\mathcal{F}_i$; and q_e is the column matrix of the elastic generalized coordinates. The column $\boldsymbol{\gamma}$ is a dummy variable chosen to satisfy $\dot{\boldsymbol{\gamma}} = \boldsymbol{\xi}$. The matrix M is the mass matrix, composed of the rigid-body mass matrix M_{rr}, the rigid-body mass matrix M_{ee} and M_{re} which are the coupling terms between the rigid-body and elastic-body behaviors. The matrix K is the stiffness matrix composed of zero matrices representing the rigid body and the coupling terms; and K_{ee}, which is the elastic-body stiffness matrix. Column matrices f_T and f_I are the external and the inertial forcing column matrices, composed of the rigid-body and the elastic-body forcing terms denoted by the subscripts r and e, respectively. Although the linear counterparts to these terms are constants, the resulting expressions from assuming large deflections result in most of the terms depending on the states. The external forcing also depends on the control input, defined as $\boldsymbol{\chi}$ here to reflect how the angular orientations of the tip vanes produce the control input.

The sail is represented as a simple FEM model composed of three element types, for which the equations describing the aforementioned matrices are derived. One such sail FEM model is shown in Fig. 3, where the sail sags described in Sec. II are incorporated as well. The three element types are as follows: Hermitian beam elements to represent the four booms, a modified natural coordinate triangular plate elements to represent the reflective sail, and a modified Hermitian beam element to represent the supporting cords. These modifications will be explained in the next section. The Hermitian beam element has the following strain-displacement relationship:

$$\epsilon_{xx} = u_x - y v_{xx} - z w_{xx} + \frac{1}{2} v_x^2 + \frac{1}{2} w_x^2 \tag{7}$$

where the subscripts x and xx denote the first and the second derivatives of a function. As per the classical theory of plates [16], the natural coordinate triangular plate element has the following strain-displacement relationship:

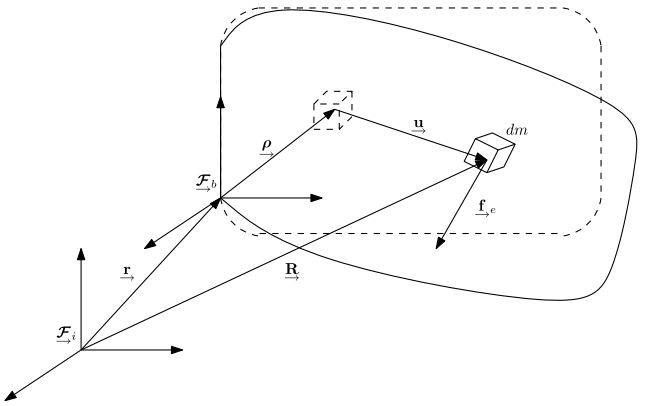

Fig. 2 Unconstrained elastic body with volume V.

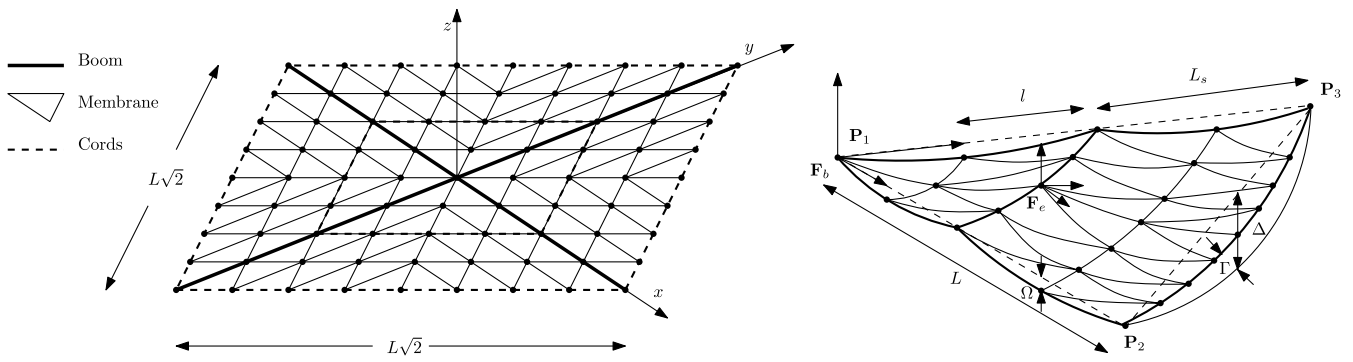

a) Sail element division **b) A triangular quadrant**

Fig. 3 Simple FEM model of the cord-mat square solar sail.

$$\epsilon_{xx} = u_x - zw_{xx} + \frac{1}{2}w_x^2,$$
$$\epsilon_{yy} = v_y - zw_{yy} + \frac{1}{2}w_y^2,$$
$$\gamma_{xy} = u_y + v_x - 2zw_{xy} + w_x w_y \tag{8}$$

All other strains are taken as zeros. These relationships are used to derive the matrices in the equations of motion.

The booms in the preceding model are fixed to the body frame origin, as are the corners of the four sail quadrants at the origin. The sail is, in theory, indirectly attached to the booms via these cords but, as seen in Fig. 3b, the membrane elements are pinned to the ends of the cords, which are also pinned to the booms. Hence, the sail is essentially pinned to the booms where the cords are pinned to the booms. In addition, the spacecraft bus is represented simply by a rigid point mass located at the bus center of mass, assuming that the effects of its deformation are likely far less significant than that of the sail.

For this research, the solution to the FEM model's equations of motion presented in Eq. (6) is provided by a Fortran-implemented version of `ode15s`, which is an ordinary differential equation (ODE) solver originally from MATLAB. The function `ode15s` uses the numerical differentiation formulas, which is a modified version of the backward differentiation formula, as described in Shampine and Reichelt [17]. To aid in solution convergence, exact solutions of the Jacobian of the equations of motion are provided. It should be noted that the matrices of the geometrically nonlinear equations of motion are state dependent. This implies that the matrices must be recalculated whenever a new state is assumed by the solver, which is a very costly process. This limits the complexity of the model, as more complex models would take infeasible amounts of time to complete the simulation.

IV. Wrinkling and Slacking Behavior of Elements

The modifications to the plate and the beam elements are needed to account for the near-incompressible nature of the thin reflective membrane and the support cords these elements are meant to represent. Specifically, these materials tend to fold upon themselves when a compressive load is applied, behaving in a nonelastic manner, whereas the elastic behavior is still preserved while in tension. To account for this change in the material behavior, three material states are defined: taut, wrinkled, and slack. The taut state refers to the case where the material is in tension about all directions. The wrinkled state refers to the case where the material is simultaneously in tension and in compression, due to varying loads about different directions. The slack state refers to the case where the material is in compression in all directions.

The topic of static and dynamic behaviors of wrinkled membranes is still an active area of research, and numerous authors have presented their solutions [18–28]. Here, an approach introduced by Miller et al. [29] is used for its mathematical simplicity and ease of integration to the FEM model. Specifically, the constitutive relationship matrix is modified based on the state of the element.

A membrane in tension as shown in Fig. 4a behaves elastically and can be modeled as a plate. Its principal stress–strain constitutive relationship can be described by

$$\begin{bmatrix}\tau_1\\ \tau_2\end{bmatrix} = \frac{E}{1-\nu^2}\begin{bmatrix}1 & \nu\\ \nu & 1\end{bmatrix}\begin{bmatrix}\epsilon_1\\ \epsilon_2\end{bmatrix} \tag{9}$$

where τ_1 and τ_2 are the major and the minor principal stresses, ϵ_1 and ϵ_2 are the major and the minor principal strains, E is Young's modulus, and ν is Poisson's ratio. This expression, when replaced with the local frame stresses τ_{xx}, τ_{yy}, τ_{xy}, and the local frame strains ϵ_{xx}, ϵ_{yy}, γ_{xy}, and simplified, result in the following expression:

$$\tau = E_t\,\epsilon = \begin{bmatrix}\tau_{xx}\\ \tau_{yy}\\ \tau_{xy}\end{bmatrix} = \frac{E}{1-\nu^2}\begin{bmatrix}1 & \nu & 0\\ \nu & 1 & 0\\ 0 & 0 & \frac{1-\nu}{2}\end{bmatrix}\begin{bmatrix}\epsilon_{xx}\\ \epsilon_{yy}\\ \gamma_{xy}\end{bmatrix} \tag{10}$$

This is the well-known plane stress–strain constitutive relationship equation, and E_t is the constitutive relationship matrix for the taut, tensioned membrane.

A membrane is considered wrinkled when it is being stretched in one direction while being compressed in another, as shown in Fig. 4b. Pure stretching occurs along the direction of the major principal stress, whereas pure compression occurs along the direction of the minor principal strain. As noted before, since a membrane under compression does not behave elastically but instead folds upon itself, the resulting minor principal stress is assumed to be zero, giving the following modified form of Eq. (9):

$$\begin{bmatrix}\tau_1\\ \tau_2\end{bmatrix} = \begin{bmatrix}E & 0\\ 0 & 0\end{bmatrix}\begin{bmatrix}\epsilon_1\\ \epsilon_2\end{bmatrix} \tag{11}$$

Once again, replacing the principal stresses and strains with the local terms and rearranging, the following constitutive relationship is derived:

$$\boldsymbol{\tau} = E_w\,\epsilon$$
$$\begin{bmatrix}\tau_{xx}\\ \tau_{yy}\\ \tau_{xy}\end{bmatrix} = \frac{E}{4}\begin{bmatrix}2(1+R) & 0 & Q\\ 0 & 2(1-R) & Q\\ Q & Q & 1\end{bmatrix}\begin{bmatrix}\epsilon_{xx}\\ \epsilon_{yy}\\ \gamma_{xy}\end{bmatrix},$$
$$R = \frac{\epsilon_{xx} - \epsilon_{yy}}{\epsilon_1 - \epsilon_2}, \qquad Q = \frac{\gamma_{xy}}{\epsilon_1 - \epsilon_2} \tag{12}$$

This is the modified constitutive relationship derived by Miller et al. [29]. The constitutive relationship matrix is E_w. Finally, a membrane is considered slack when it is being compressed in both principal directions. In a pure slack state, stresses remain zero throughout; that is, the constitutive relationship matrix is simply $E_s = \mathbf{0}$.

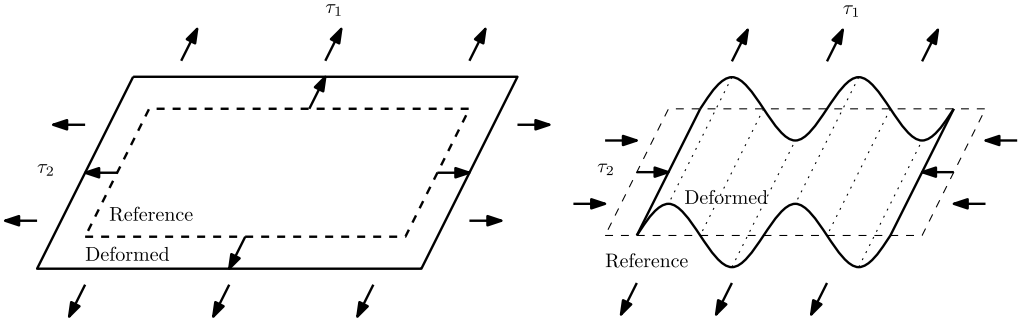

a) Tensile stress **b) Compressive stress**

Fig. 4 Membrane under varying stress conditions.

Now, all three cases can be described in combination by using the following principal stress–strain constitutive relationship as the starting point:

$$\begin{bmatrix} \tau_1 \\ \tau_2 \end{bmatrix} = \frac{E}{1-ab\nu^2} \begin{bmatrix} b & ab\nu \\ ab\nu & a \end{bmatrix} \begin{bmatrix} \epsilon_1 \\ \epsilon_2 \end{bmatrix} \tag{13}$$

where the constants a and b are modified based on the state of the material. Replacing the principal stresses and strains with the local terms and rearranging, we have

$$\begin{bmatrix} \tau_{xx} \\ \tau_{yy} \\ \tau_{xy} \end{bmatrix} = \frac{E}{4(1-ab\nu^2)} \times \begin{bmatrix} 2[a(1-R)+b(1+R)] & 4ab\nu & Q(b-a) \\ 4ab\nu & 2[b(1-R)+ab(1+R)] & Q(b-a) \\ Q(b-a) & Q(b-a) & b+a-2ab\nu \end{bmatrix} \times \begin{bmatrix} \epsilon_{xx} \\ \epsilon_{yy} \\ \gamma_{xy} \end{bmatrix} \tag{14}$$

When $a = b = 1$, the preceding equation becomes equivalent to Eq. (10), i.e., the plane stress constitutive relationship. When $a = 0$ and $b = 1$, the preceding equation simplifies to Eq. (12), i.e., the wrinkled stress–strain constitutive relationship. When $a = b = 0$, the preceding simply becomes $\mathbf{0}$, i.e., the slack stress–strain constitutive relationship. Hence, all three material states can be represented with the appropriate values of a and b. In theory, the degree of wrinkledness and slackness can be classified by the values of a and b, where a controls the degree of wrinkledness and b controls the degree of slackness of the material. However, this particular extension is not used for this research due to the simulation instability it brings.

The criterion that determines the state of the material can be summarized as follows:

$$\begin{cases} a = 1, & b = 1 & \text{if } \varsigma_1 \geq 0 \\ a = 1, & b = \delta & \text{if } \varsigma_2 \geq 0 \text{ and } \varsigma_1 < 0 \\ a = \delta, & b = \delta & \text{if } \varsigma_2 < 0 \end{cases} \tag{15}$$

where $\varsigma_1 = \epsilon_2 + \nu\epsilon_1$, $\varsigma_2 = \epsilon_1$, and δ is a small number near zero. This criterion is also known as the stress–strain criterion in the literature. Two other criteria for determining the material state are known, the stress criterion and the strain criterion, but Kang and Im [27] showed that the stress criterion and the strain criterion tend to be less accurate than the mixed criterion; hence, the stress–strain criterion is used. Keeping the values of parameters a and b nonzero accounts for the idea that, even during compression, the membrane still must be subjected to a finite force before it folds upon itself. This also prevents the physical impossibility where the membrane would continue to fold in upon itself after an initial impulse forcing, due to no resistance being present.

A similar modification to the constitutive relationship for the beam elements is made. A string being compressed along its length will simply collapse as opposed to providing elastic resistance, just as a membrane would. The only difference is that, unlike a membrane, a string is one-dimensional and such a compressive load immediately results in a slacked state. A wrinkled state has no physical meaning for a string. Given its one-dimensional nature, the constitutive relationship can be modified in a following manner for the slacked state:

$$\tau = bE\epsilon \tag{16}$$

where b is equivalent to the slacking parameter for the membrane. Logical dissemination of the modified constitutive relationship is that, when the string is under compressive loading, its stiffness is modified to represent the near-zero resistance the string provides against the compression.

V. Solar Radiation Pressure Force on the Sail

For the purpose of this research, the membrane is assumed to have ideal optical properties, where all of the incident solar radiation is specularly reflected off a flat surface. In addition, each membrane element is assumed to be flat for the purpose of calculating the solar radiation pressure force.

The combination of the momentum transported by the photons and the reaction provided by the reflected photons results in a force vector that is always normal to the flat surface, as shown in Fig. 5. The unit vector from the sun to a point on the surface is $\hat{\boldsymbol{s}}$. The unit normal vector for the reflective surface is $\hat{\boldsymbol{n}}$, the resulting SRP force $\boldsymbol{f}_{\text{ideal}}$ is in the opposite direction of the unit normal, and the angle from $\hat{\boldsymbol{n}}$ to $\hat{\boldsymbol{s}}$ is α, which is also known as the cone angle. Assuming A to be the area of the reflected surface and P to be the pressure exerted on the surface by the SRP, the force exerted on the reflective surface due to the SRP is [6]

$$f_{\text{ideal}} = -2PA(\hat{s}^T\hat{n})^2\hat{n} \tag{17}$$

The value of the SRP is typically taken to be $P = 4.56\times10^{-6}\,\text{N}\cdot\text{m}^{-2}$ at one astronomical unit (AU) from the sun. However, for emphasis on the flexible dynamics and to consider cases of missions closer to the sun, P is taken to be $1.8253\times10^{-5}\ \text{N}\cdot\text{m}^{-2}$ instead, corresponding to the SRP at 0.5 AU away from the sun.

McInnes also derives the SRP forces produced by optically nonideal surfaces in his book [6]. Using optical properties derived in the California Institute of Technology, Jet Propulsion Laboratory (JPL) comet Halley rendezvous study, one can show that the ideal optical model and the nonideal optical model differ in the SRP forces produced by up to 10%, where the difference is the greatest when the surface normal is parallel to the sun and the least when the surface normal is perpendicular to the sun.

To calculate the SRP forces for the sail, $\hat{s}$ and $\hat{n}$ should be represented in the same frame. Here, the body frame is assumed to be the common frame in which the forces are calculated, denoted by the subscript b. Since the sail is expected to billow as the simulation progresses, the value of $\hat{\boldsymbol{n}}_b$ is expected to be different at different points on the sail and at different points in time. Fortunately, the sail is already divided into finite membrane elements, and the simulator would need to recalculate the terms of the equations of motion at every state change, as noted previously. Hence, $\hat{\boldsymbol{n}}_b$ is determined for each element whenever the simulator changes the state variable; then, it is used to recalculate the SRP force on the sail.

Determination of the reflective sail's orientation can be simplified by taking advantage of the shape of the membrane element. Specifically, assuming that each element surface is flat for the purpose of calculating the SRP force, the three vertices of a triangular element can describe a unique three-dimensional plane, from which a

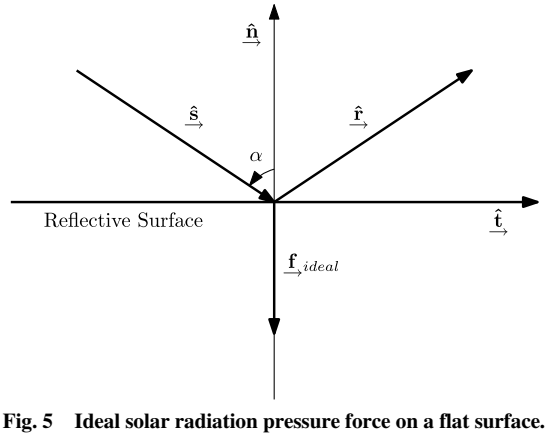

Fig. 5 Ideal solar radiation pressure force on a flat surface.

constant normal vector can be derived to describe the orientation of the element as a whole. This trait is not true for any element with less than three vertices, for which there are an infinite number of normal vectors for any point on the element, or for any element with more than three vertices, for which any plane through all of its arbitrarily positioned vertices must be curvilinear.

It is assumed that the location of the sun in the inertial frame is known by the sun vector in the inertial frame $\hat{s}_i$ and its body frame counterpart $\hat{s}_b = C_{bi}\hat{s}_i$, where C_{bi} is the inertial to body frame rotation matrix and is known. The normal vector of a flat triangular element is simply a cross product of two vectors formed from the three vertices of the triangle. Specifically, letting $\boldsymbol{p}_i$ be the location of node i of the triangular element in the body frame (that is,

$$\boldsymbol{p}_i = \boldsymbol{\rho}_i + \boldsymbol{u}_i \tag{18}$$

where $\boldsymbol{\rho}_i$ is the original location of the node and $\boldsymbol{u}_i$ is the elastic deformation of the node), the normal vector in the body frame can be written as

$$\boldsymbol{n}_b = (\boldsymbol{p}_2 - \boldsymbol{p}_1)^{\times}(\boldsymbol{p}_3 - \boldsymbol{p}_1) \quad \hat{n}_b = \frac{n_b}{\|n_b\|} \tag{19}$$

Hence, with the knowledge of $\hat{s}_b$ and $\hat{n}_b$, the SRP force in the body frame can be calculated for any set of triangular element nodes. In Eq. (19), we have employed the $(-)^{\times}$ superscript to implement the vector cross product using the matrix

$$p^{\times} = \begin{bmatrix} 0 & -p_3 & p_2 \\ p_3 & 0 & -p_1 \\ -p_2 & p_1 & 0 \end{bmatrix} \tag{20}$$

where $\boldsymbol{p} = [\, p_1 \quad p_2 \quad p_3 \,]^T$.

VI. Sail Shadowing

Since a solar sail relies on the sun being shone on its reflective surface to harness the momentum from the photons, problems arise when the sail becomes shadowed. In particular, when a portion of the sail is shadowed by some part of itself due to its orientation with respect to the direction of the sun, it operates with reduced total thrust force and any asymmetry in the shading pattern leads to disturbance torques that adversely affect its attitude profile. In this section, we consider the determination of shaded areas on a sail due to another part of the spacecraft. The main contribution of this section is the verification of the common assumption that the effect of sail shadowing is minimal on the general attitude profile of the solar sail.

Determining the shaded area is essentially a problem of projecting the shadowing component onto the reflective sail. Assuming that the component is opaque, the following three pieces of information are needed to perform this projection: the Cartesian location of the component's outer shell, the sun vector, and the plane in which the sail resides. For simplicity, assume that the component is convex and that its outer shell can be described by a finite number of vertices, which are known in the body frame. The sun vector $\hat{s}$ is also assumed to be known in the body frame. With the FEM model, the sail membrane is represented as a collection of triangular elements, and the nodes forming the vertices of these elements can be used to define a unique Cartesian plane onto which the outer shell can be projected. The goal is to find a set of points that describes the outer boundary of the projected shadow on that portion of the sail.

Assuming that the coordinates of the triangular vertices are known in the body frame, the projection plane can be defined entirely by a normal vector from its origin. To find the boundaries of the shadow due to the component, its vertices are first projected onto this projection plane. The projected vertices, then defined in the plane as two-dimensional coordinates, can be used to determine the convex hull of the set, which by definition defines the set of points representing the outer hull of a larger set of points that forms a convex shape. For the purpose of this research, this is performed by using the gift-wrapping algorithm, also known as the Jarvis march [30]. Once the convex hull is defined, the same process used to determine the convex hull can also be applied to the individual nodes of the element, or any other point on the surface defined by those nodes, to determine whether they are within the convex hull or not. Any nodes within the convex hull are assumed to be shaded, hence not producing any thrust.

Two particular cases of shading are considered in this research. The first case is the shadowing on the sail due to the bus structure, shown in Fig. 6a. This is a very simple case where a small number of vertices representing the bus structure is checked against each of the triangular membrane elements to determine whether the individual nodes are within the shadow of the bus structure. Figure 6b shows the sail plane of the triangular element shown in Fig. 6a, where the shaded and the unshaded nodes are marked based on whether the node is within or outside of the projected bus convex hull. Assuming one bus structure shading the sail, the previously described process has to be performed only once per element per time step, and hence is integrated into the simulation with only small computational overhead.

The second case is the shadowing on the sail due to itself. In this case, each element is assigned three points that are halfway between the centroid and the vertices. The shadowed area is determined by the nodes of the shadowing element projected onto the plane formed by the shadowed element. The points being tested for being shadowed, however, are the newly assigned points previously mentioned. This is

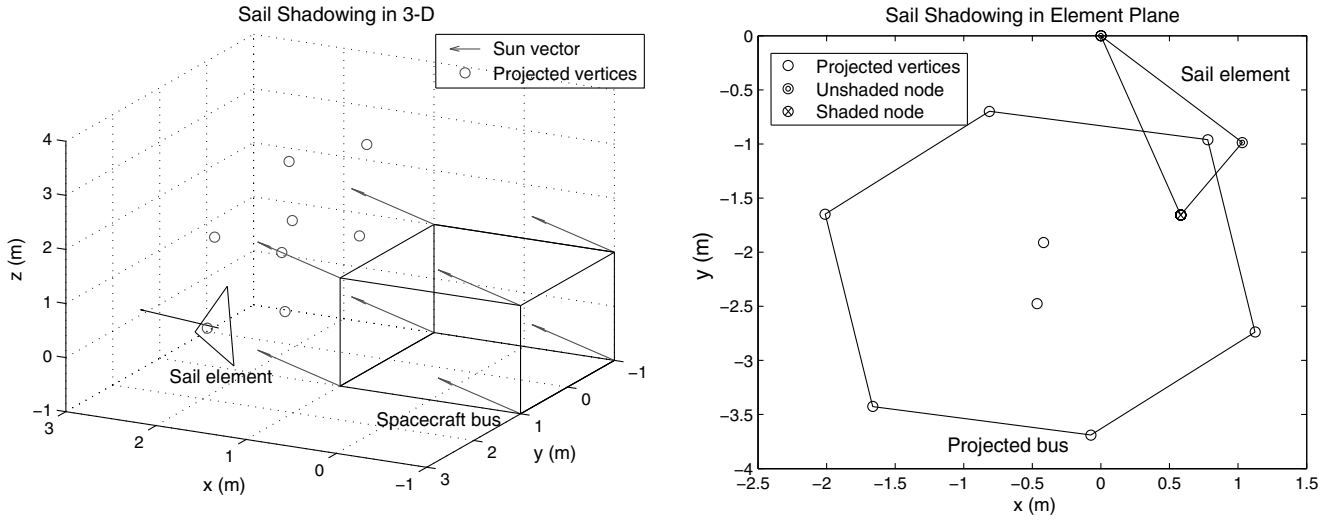

a) b)

Fig. 6 Sail shadowing due to bus structure.

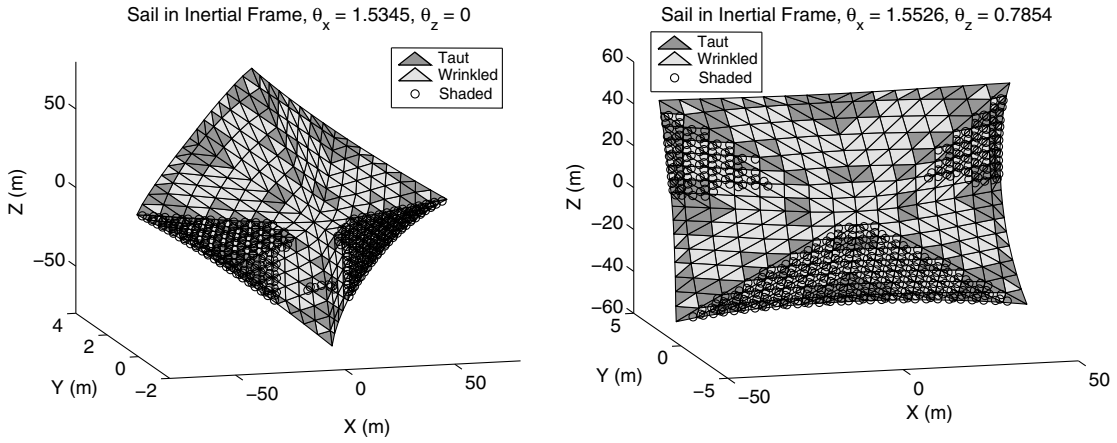

a) $\theta_x = 1.5345$, $\theta_z = 0$ **b)** $\theta_x = 1.5526$, $\theta_z = 0.7854$

Fig. 7 3-D plot of sail in inertial frame with shadowing due to sail membrane.

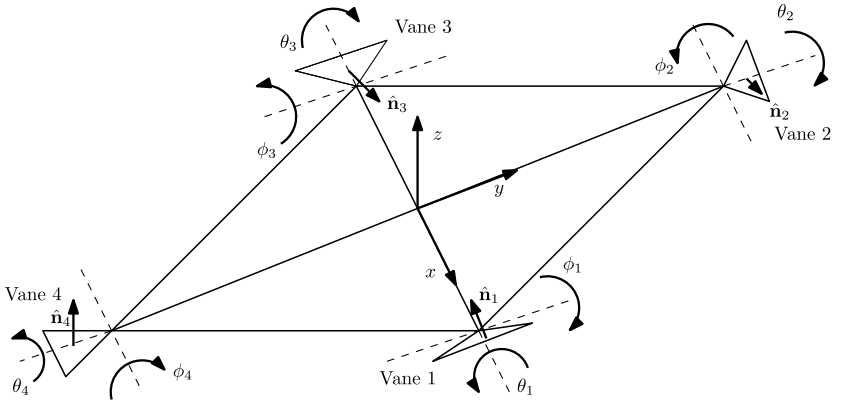

Fig. 8 Two-DOF vane configurations.

necessary in order to prevent overlap issues associated with elements shadowing adjacent elements. Sample results of testing the sail shadowing in near-edge-on cases are demonstrated in Fig. 7, where the circles represent the points shadowed by the sail. This case is here simply for demonstrative purposes however, because the computational cost of checking the possibility of shadowing due to another membrane element for every membrane elements is prohibitively expensive for the simulation. Hence, this check is not included in the simulation.

VII. Vane Design and Control Allocation

Attitude control actuation for the sail is performed by four vanes attached to the tips of the supporting booms. These vanes reflect the incoming photons just as a sail would, and they use the resulting thrust and its position with respect to the sail center to produce attitude-controlling torques. For the purposes of this research, the orientations of the vanes are defined via two angular degrees of freedom (DOFs) θ_i and ϕ_i for $i = 1..4$, as shown in Fig. 8. To be specific, vane 1 is rotated along the body x axis by θ_1, followed by a rotation along the rotated y axis by ϕ_1. Other vanes follow the same convention in terms of the order of rotation. The setup described here is a physically achievable actuation scheme where two angular actuators are attached sequentially.

To simplify the calculation of the torques produced by these vanes, the following assumptions are made: first, it is assumed that the booms are rigid and positioned about the body frame axes as Fig. 8 depicts. Second, the changes in the center of pressure of the vanes when tilted are neglected. Third, the reflective surface of the vane is assumed to be rigid and flat.

In a three-dimensional (3-D) space, the sun vector is represented by not only the cone angle α but also by the clock angle β, as shown in Fig. 9. The sun vector in the sail body frame can then be written as

$$\hat{s}_b = \begin{bmatrix} S_\alpha C_\beta \\ S_\alpha S_\beta \\ -C_\alpha \end{bmatrix} \tag{21}$$

where S and C represent sine and cosine functions, respectively. Using this, the SRP force equation, and the body frame to vane frame rotation matrix $C_{vb,1}$ defined as the successive rotations of θ_1 and ϕ_1, the normalized torque produced by vane 1 in the body frame can be written as

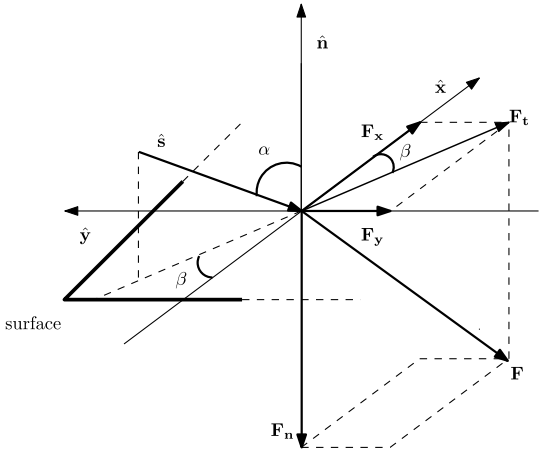

Fig. 9 Three-dimensional representation of solar radiation pressure force.

$$\hat{G}_{b1} = \begin{bmatrix} 0 \\ C_{\phi 1} C_{\theta 1} \\ C_{\phi 1} S_{\theta 1} \end{bmatrix} (S_{\phi 1} S_\alpha C_\beta - C_{\phi 1} S_{\theta 1} S_\alpha S_\beta - C_{\phi 1} C_{\theta 1} C_\alpha)^2 \quad (22)$$

Similar expressions can be written for torques produced by other vanes. The total control torque offered by the vanes is the combination of the torque equations, and it is a complex nonlinear equation of eight control variables that output three components. An analytical solution to the problem of deriving the eight angles from a given torque value is unlikely and, due to its nonlinearity, conventional means of solving nonlinear equations are met with failure.

This problem involves eight control variables and three unknowns: an underconstrained control allocation problem. A method was created by the authors in order to solve this problem, which uses an estimation to the boundaries of the attainable moment set (AMS), which is the set of torques that can be produced by the vanes, to redefine the problem into an affine numerical portion and a solvable analytical portion [31]. The details of the process are omitted in this paper, but the algorithm essentially accepts any desired torque and the current sun angles as an input, and it outputs a set of vane angles that will produce the desired torque (or a scalar-scaled version of it if the desired torque is not physically achievable by the vanes).

Figure 10 shows an example execution of the algorithm. On this figure are the individual vane AMSs, its estimation by ellipses, the combined estimated AMS, and a solution set of vane torques generated by the numerical portion of the process for the normalized torque $\hat{G}_d = [0.5, 0.3, 1.3]$ and the sun angles $\alpha = 0$ and $\beta = 0$. The marked points are the torques produced by each vane, and it can be seen that the torques do add up to $\hat{G}_d$ as desired. With the individual vane torques known, the analytical portion of the process calculates the individual vane angles to be $\phi_1 = -0.1067$, $\theta_1 = 0.6073$, $\phi_2 = 0.1365$, $\theta_2 = 0.9647$, $\phi_3 = -0.0231$, $\theta_3 = -0.8952$, $\phi_4 = 0.1148$, and $\theta_4 = -0.4841$. These angles can then be used by the actuators to tilt the vanes to produce the desired torques.

VIII. Control Law and Simulation Steps

The completion of the control system requires a control law. For robustness and simplicity, we use the quaternion (Euler parameter) PD control law to determine to desired control torques for the system. Hence, let the desired control torque in the body frame G_d be given by

$$G_d = -K_d \boldsymbol{\omega} - k_p \boldsymbol{\epsilon}_e \quad \boldsymbol{\epsilon}_e = (\eta_d 1_3 - \boldsymbol{\epsilon}_d^\times)\boldsymbol{\epsilon}_n - \boldsymbol{\epsilon}_d \eta_n \quad (23)$$

where $\boldsymbol{\epsilon}_e$ is the vector component of the error quaternion, $\boldsymbol{\epsilon}_d$ and η_d are the vector and the scalar components of the desired quaternion, and $\boldsymbol{\epsilon}_n$ and η_n are the vector and the scalar components of the current quaternion. The current quaternion is known by the kinematics relationship with the angular velocity, which is calculated alongside the equations of motion.

The current quaternion can be determined from the kinematics relationship involving the angular velocity and is integrated alongside the equation of motion:

$$\dot{\boldsymbol{\epsilon}}_n = \frac{1}{2}(\boldsymbol{\epsilon}_n^\times \boldsymbol{\omega} + \eta_n \boldsymbol{\omega}) \quad (24)$$

$$\dot{\eta}_n = -\frac{1}{2}\boldsymbol{\epsilon}_n^T \boldsymbol{\omega} \quad (25)$$

It should be noted that the quaternion PD control law has been shown to be globally asymptotically stable in controlling the attitude of a rigid body [32]. Here, we will extend this result to the local asymptotic stabilization of a linearized flexible sail model.

Let us linearize Eq. (6) about the equilibrium $\boldsymbol{\xi} = \dot{q}_e = q_e = \boldsymbol{\epsilon}_e = \mathbf{0}$ and $\eta_e = 1$. Setting $f_I(q, \dot{q}) = \mathbf{0}$ and taking $f_T(q, \boldsymbol{\chi}) = \bar{B} f_c(t)$, where $\bar{B} = [\mathbf{0}_{3\times 3} \quad 1_3 \quad \mathbf{0}_{3\times N_c}]^T$ (1_3 is the 3×3 identity matrix), the linearized motion equation becomes

$$\bar{M}\,\ddot{q} + \bar{D}\,\dot{q} + \bar{K} q = \bar{B} G_d \quad (26)$$

This assumes that the control torque is applied to a (perhaps vanishingly small) rigid body at the mass center. Here, we have defined $\bar{M} = M(\mathbf{0})$ and $\bar{K} = K(\mathbf{0})$, and we introduced a damping matrix of the form

$$\bar{D} = \begin{bmatrix} 0 & 0 \\ 0 & D_{ee} \end{bmatrix} \quad (27)$$

We will assume a Rayleigh damping model of the form $D_{ee} = mM_{ee} + kK_{ee}(\mathbf{0})$, which is symmetric and positive definite if $m > 0$ and $k > 0$.

In an effort to establish the stability properties of the equilibrium, we introduce the Lyapunov function candidate:

$$\begin{aligned} V &= \frac{1}{2}\dot{q}^T \bar{M}\,\dot{q} + \frac{1}{2} q^T \bar{K} q + k_p[\boldsymbol{\epsilon}_e^T \boldsymbol{\epsilon}_e + (\eta_e - 1)^2] \\ &= \frac{1}{2}\dot{q}^T \bar{M}\,\dot{q} + \frac{1}{2} q_e^T K_{ee}(\mathbf{0}) q_e + 2k_p(1 - \eta_e) \end{aligned} \quad (28)$$

Differentiating V and using the motion equations in Eqs. (25) and (26) yields

$$\begin{aligned} \dot{V} &= \dot{q}^T(\bar{M}\,\ddot{q} + \bar{K} q) - 2k_p \dot{\eta}_e \\ &= -\dot{q}_e^T D_{ee} \dot{q}_e + \dot{q}^T \bar{B} G_d - 2k_p(\boldsymbol{\epsilon}_d^T \dot{\boldsymbol{\epsilon}}_n + \eta_d \dot{\eta}_n) \\ &= -\dot{q}_e^T D_{ee} \dot{q}_e + \boldsymbol{\omega}^T G_d - 2k_p \boldsymbol{\epsilon}_d^T \left(\frac{1}{2}\boldsymbol{\epsilon}_n^\times \boldsymbol{\omega} + \frac{1}{2}\boldsymbol{\omega}\eta_n\right) - k_p \eta_d \boldsymbol{\omega}^T \boldsymbol{\epsilon}_n \end{aligned}$$

Substituting for G_d from Eq. (23) and simplifying leads to

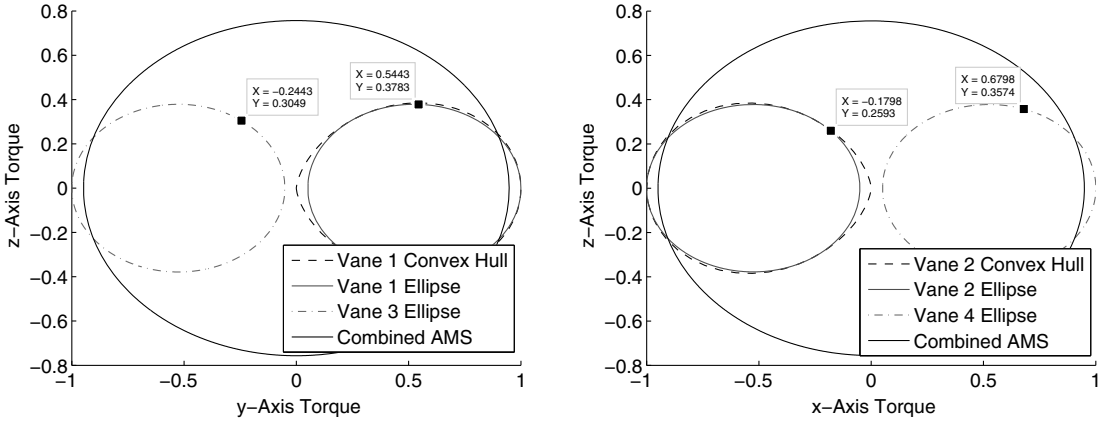

a) Vanes 1 and 3 b) Vanes 2 and 4

Fig. 10 Estimated AMS and the results of the algorithm for $\hat{G}_d$ = [0.5,0.3,1.3] with $\alpha = 0$ and $\beta = 0$.

$$\dot{V} = -\dot{q}_e^T D_{ee} \dot{q}_e - \boldsymbol{\omega}^T K_d \boldsymbol{\omega} \leq 0 \tag{29}$$

Applying the Krasovskii–LaSalle theorem, the invariant set consistent with $\boldsymbol{\omega} = \dot{q}_e = 0$ is $\boldsymbol{\omega} = v = \dot{q}_e = q_e = \boldsymbol{\epsilon}_e = \mathbf{0}$, which establishes local asymptotic stability of the equilibrium.

Although the control law in Eq. (23) has been shown to yield local asymptotic stability, this can be compromised by several factors. The saturation imposed by the vanes has not been taken into account. Furthermore, the control torque is not realized by "rigid torques" applied to a central rigid bus structure. As will be discussed in the following, it is realized by SRP forces acting on the tip vanes that are not collocated with the central bus. This lack of collocation between the spatial locations for applying the SRP forces (on the vanes) and sensed attitude variables (the angular velocity and quaternions of a central bus structure) can lead to instability. One of the main contributions of the papers is to assess the possibility of this happening.

The control gains K_d and k_p are intentionally tuned such that torques several magnitudes higher than what the vanes are capable of producing are generated until the sail attitude is near the desired attitude. The feasibility portion of the control allocation algorithm automatically scales the requested torque into maximum values that can be achieved by the vanes. The control law would see comparably minimal changes on the attitude and continue to request the same extremely high torque values, holding the vane in the orientation that produces the maximum torque in the desired direction. This setup allows relatively fast slewing maneuvers to be performed. Since the solar sail's thrust direction and power are directly related to its attitude, the fast slewing capacity for the controller is a highly desired one.

The attitude control as a whole can then be described as depicted in Fig. 11. The attitude control simulation is performed by deriving a desired control torque from the PD control law, feeding it through the control allocation algorithm to scale the control torque and derive the vane angles required to achieve the scaled control torque, and then passing the vane angles along to the dynamics simulator to calculate the vane forces and torques. The state integration of the dynamics equation for the current time step is performed to derive the next set of attitude profiles, which the PD control uses to update its desired control torque.

The detailed description of each step is as follows: first, the PD control law described previously is used in conjunction with the current attitude profile of the sail to derive a desired control torque. For the first simulation, initial values for $\boldsymbol{\omega}$ and $q_n = \epsilon_n$ (along with the generalized coordinates) are user specified, whereas the consecutive runs are performed with the results from the previous run of the ODE solver.

The desired control torque from the PD control law is then scaled by the area of the vane and the solar radiation pressure constant to take into account the force normalization performed when deriving the control allocation method, i.e., $\hat{G}_d = G_d/(2PA)$. This scaled desired torque and the sun vector in the body frame with the representative sun angles are used as inputs to the control allocation process described in Sec. VII to derive the eight vane angles. The vane angles are used instead of the torques derived by the process to properly take into account the discrepancy that occurs by the flexibility of the booms the vanes are attached to. The body frame sun vector $\hat{\boldsymbol{s}}_b$ is calculated using the rotation matrix derived from the quaternions, i.e.,

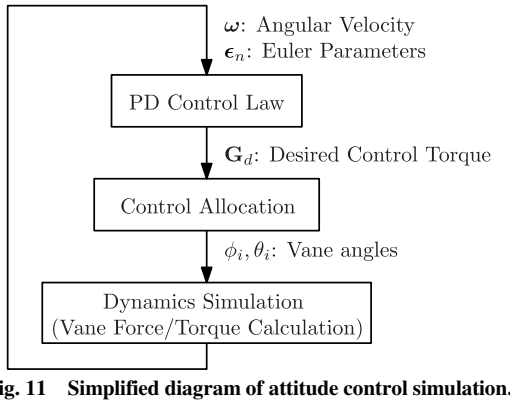

Fig. 11 Simplified diagram of attitude control simulation.

$$\hat{\boldsymbol{s}}_b = C_{bi}\hat{\boldsymbol{s}}_i \quad C_{bi} = (1 - 2\boldsymbol{\epsilon}_n^T\boldsymbol{\epsilon}_n)1_3 + 2\boldsymbol{\epsilon}_n\boldsymbol{\epsilon}_n^T - 2\eta_n\boldsymbol{\epsilon}_n^\times \tag{30}$$

where $\boldsymbol{\epsilon}_n$ and η_n are the quaternion components from either the previous simulation or the specified initial value.

It should be noted that there is a duplication of information when providing both the sun vector and the sun angles, and this is mainly due to the current implementation using the sun vector to calculate the forces, but with the solution to the single-vane problem being designed around the sun angles. The derivation of the sun angles from the sun vector is straightforward when considering Eq. (21): $\alpha = \cos^{-1}\hat{s}_b(3)$ and $\beta = \text{a tan } 2(\hat{s}_b(2), \hat{s}_b(1))$, $\alpha \neq 0$. If $\alpha = 0$, then the value of β cannot change the orientation of the sun vector, and hence is set to zero.

Once the vane angles are known, the next time step of the nonlinear dynamics simulation can be simulated using the ODE solver, as noted in Sec. III. An additional process is added onto the functions being integrated: that of calculating the force due to the vanes at the ends of each boom. The SRP force due to the vane is calculated with Eq. (17), using the vane's normal vector and the sun vector in the body frame. The sun vector is calculated in the same manner as before, whereas the vane's normal vector is calculated using the following assumptions:

1) Each vane is aligned with the line formed by the last two nodes of the boom the vane is attached to (this frame is referred to as the deformed frame henceforth).

2) Vane rotations are performed at the deformed frame.

3) Vane rotations do not cause force center translation, which is assumed to be at the tip of the boom. Given the preceding assumptions, the calculation of the vane normal can be devolved into finding two rotation matrices: one that rotates the vane frame to the deformed frame, and another that rotates the deformed frame to the body frame. The first of these, C_{dv}, is calculated using the same set of rotation matrices used to calculate the torques in the control allocation problem, specifically,

$$C_{dv} = \begin{cases} (C_{y,\phi_1}C_{x,\theta_1})^T & \text{for vane1} \\ (C_{x,\phi_2}C_{y,\theta_2})^T & \text{for vane2} \\ (C_{y,\phi_3}C_{x,\theta_3})^T & \text{for vane3} \\ (C_{x,\phi_4}C_{y,\theta_4})^T & \text{for vane4} \end{cases} \tag{31}$$

where $C_{i,\theta}$ is a principal rotation of θ about the i axis. These rotations are consistent with the DOFs shown in Fig. 8 from the control allocation section (Sec. VII). The rotation matrix from the deformed frame to the body frame is calculated by noting that the rotation between two vectors is easily found by taking the cross product of the two vectors to find the axis of rotation, with its angle of rotation found from the dot product of the two vectors. Specifically, C_{bd} is calculated by

$$\begin{aligned} C_{bd} &= (\cos(\varphi)1_3 + (1 - \cos(\varphi))\hat{a}\hat{a}^T - \sin(\varphi)\hat{a}^\times) \\ \hat{a} &= \frac{a}{\|a\|}, \qquad a = \hat{t}^\times\hat{n}_r, \qquad \varphi = \cos^{-1}(\hat{t}\cdot\hat{n}_r) \\ \hat{t} &= \frac{t}{\|t\|}, \qquad t = \boldsymbol{p}_2 - \boldsymbol{p}_1 \\ \hat{n}_r &= \begin{cases} [1\,0\,0]^T & \text{for vane 1} \\ [0\,1\,0]^T & \text{for vane 2} \\ [-1\,0\,0]^T & \text{for vane 3} \\ [0\,-1\,0]^T & \text{for vane 4} \end{cases} \end{aligned} \tag{32}$$

where $\boldsymbol{p}_i$ are the deformed coordinates of the last two nodes of the boom in the body frame. Once the body frame sun vector and the vane

normal vectors are known, the solar radiation pressure force can be calculated.

The force due to the vane is assumed to be a point force on the edge of the boom: in terms of the dynamics simulation, the resulting generalized force vector is written as follows:

$$f_{T,v} = [F_v^T \quad G_v^T \quad f_{e,v}^T]^T \quad F_v = 2PA(\hat{s}_b \cdot \hat{n}_{v,b})^2 \hat{n}_{v,b}$$
$$G_v = p_2^{\times} F_v \quad f_{e,v} = \tilde{P}_{v2}^T F_v \quad \tilde{P}_{v2} = [\mathbf{0}_{3\times 6} 1_3 \mathbf{0}_{3\times 3}] \tag{33}$$

where $\boldsymbol{p}_2$ denotes the deformed coordinate of the boom edge. The element generalized force vector $f_{e,v}$ must be placed in the appropriate index of the global generalized force vector to affect the edge node as intended, whereas F_v and G_v are simply added to the existing rigid-body generalized force.

The PD control law acts outside of the ODE solver, but the control force provided by the vanes is calculated alongside the SRP force due to the sail and is dynamically modified within the ODE solver. The flexibility of the points in which the vanes are attached to causes changes in the control torque generated by the vanes even when the vane angles are not changing. This is a plausible on-orbit scenario, as the on-orbit controller may only be able to provide control vane angles at prespecified intervals due to electronic hardware limitations or for stability reasons. The simulation captures this dynamic with its continuous update to the control torque based on a fixed vane angle within a fixed time step. The other realistic addition to the controller setup would have been implementing command and actuation delays, but these have been omitted here for simplicity.

The remaining details of the dynamics simulation are equivalent to those introduced in Secs. III and IV. The ODE solver provides the generalized displacement and the attitude information of the system at the next time step, and then the wrinkling criterion uses the updated principal stresses and strains to determine the sail membrane's current state and updates the constitutive relationship matrix appropriately. This process repeats itself with the newly found states until a designated time step is reached.

It is worthwhile to note that the controllability problem of the vane actuators have been considered as well. By linearizing the equations of motion and the vane actuation equation about the states and the vane angles, and then using the system controllability theorem presented by Hughes and Skelton [33], one can show controllability of the sail for low-frequency modes given a number of arbitrary pointing orientations and their steady-state elastic deformations. The details of this simulation process and its results can be found in the Choi's thesis [15].

IX. Sail Simulation

To demonstrate the capability of the controller and the simulator, a simple attitude pointing problem is defined: rotate a steady-state cord-mat solar sail to a prescribed orientation defined by a z-y-x Euler rotation by using the previously described control method. The simulation is performed for a designated period of time, which is chosen to show the sail settling down on the desired attitude profile.

The sail and the vane control actuation designs are as described prior to this section, with the following dimensions: $L = 70.7$ m, $\Delta = \Omega = 1 \times 10^{-2}$, and $\Gamma = 0.0608$. The structural parameters are given in Table 1. The vanes are assumed to be a right isosceles triangle with a side length of 12.5 m. This seems excessively large, but it is a necessary sizing requirement to counteract the disturbance torques produced by the sail, as will be explained later on in this section. A bus with a dimension of $10 \times 10 \times 10$ m is assumed to be located at the center of the sail. The bus is intentionally sized large to better see the effects of sail shadowing due to it. As mentioned previously, sail shadowing due to itself has not been implemented for the simulation due to its excessive computational load.

A Rayleigh damping model is used, i.e., $D_{ee} = mM_{ee} + kK_{ee}(0)$, where m and k are the damping parameters. For this simulation, damping parameter values of $m = 1$ and $k = 1 \times 10^{-5}$ are used: a choice based on trial and error.

Table 1 Structural parameters for the cord-mat square solar sail

	Beams		Triangular plate	
	Sail boom	Support cord		Sail membrane
E, N/m^2	2.87×10^{10}	6.619×10^{10}	E, N/m^2	4×10^9
A, m^2	2.87×10^{-5}	2.191×10^{-7}	ν	0.3
I, m^4	1.6104×10^{-7}	3.8201×10^{-15}	h, m	1×10^{-5}
ρ, kg/m^3	1440	1440	ρ, kg/m^3	1392

Table 2 Commanded Euler angle orientations and control gains used

Euler angles			Control gains	
θ_x	θ_y	θ_z	k_p, N · m/rad	K_d, N · m/rad/s
$\frac{\pi}{2}$	0	0	5×10^5 P	$2.5 \times 10^2 k_p 1_3$
$\frac{\pi}{4}$	0	$\frac{\pi}{4}$	1.5×10^6 P	$1.6 \times 10^2 k_p 1_3$

The sail is preloaded by SRP with the sun vector $\hat{s}_i = [0 \quad 0 \quad -1]^T$ and stabilized before the controller is enabled. The simulation begins at 6000 s: when the preloading simulation ends with the vane control algorithm enabled. The simulation is performed for 7500 s, with 50 s in between each time step for a total of 150 time steps. Two attitude profiles are presented here with varying controller gains: $\theta_y = \theta_z = 0$ with $\theta_x = \pi/2$, and $\theta_z = \pi/4$, $\theta_y = 0$ with $\theta_x = \pi/4$. Different control gains are used for each simulation, as listed in Table 2. These gains are chosen by a trial-and-error process to minimize settling time and overshoot. Note that the gains are scaled by P, which is the SRP constant.

Figure 12 shows the resulting sail shape in the body frame and the Euler angle rotation of the sail's attitude when commanded to an edge-on configuration. The end shape of the sail is very close to that of the sail without any SRP force loads. This is an expected behavior, as the SRP force is minimal against a reflective surface edge-on to the sun. The sail attitude converges to the desired attitude in a reasonably rapid fashion, reaching a 99% settling time (time taken to reach 99% norm of the desired attitude) within 4000 s. It is worthwhile to note that there is an odd "wriggling" of θ_x during the slewing process. It should also be noted that, although the membrane element nodes along the negative y axis were marked to be shaded, the entire region quickly stopped producing any SRP force due to the sail elements facing away from the sun.

The aforementioned odd behavior can be explained by observing Fig. 13. In particular, note how the sail experiences a significant disturbance torque resisting the rotation induced by the controller. Dubbed the "shuttlecock" effect, this is a phenomenon where the slanted shape of each sail quadrant, combined with the nature of the reflective surface to produce more SRP force when face-on toward the sun, results in a restoring torque that tries to keep the spacecraft in a sunward direction. As observed in Fig. 13a, this disturbance torque grows as the sail is tilted, until it reaches the peak torque just before $\theta_x = \pi/4$, and then it starts to fall off gradually until it is near zero when the sail is edge-on. The peak disturbance torque is very large: the vanes are only capable of producing, at most, 0.28 N · m along the x or y axis, leaving around 0.05 N · m of excess torque to control the spacecraft after counteracting the disturbance in worst cases. This disturbance is likely to drive the sizing requirement for the vanes.

The predicted and the actual control torques produced by the vanes are given in Fig. 13b. The difference occurs due to the bending experienced by the boom, which is not part of the mathematical model used to derive the vane angles but is part of the simulation due to the structural dynamics simulated. However, it can be seen that the difference between the two is minimal. When the sail is face-on toward the sun, the difference between the two torques are visible in the plot, reflecting how the SRP force bends the booms significantly when the sail is face-on to the sun. As the sail is tilted to the edge-on orientation, the plot demonstrates how the difference between the predicted and the actual control torques are reduced. The difference eventually becomes insignificantly small as the sail becomes edge-on

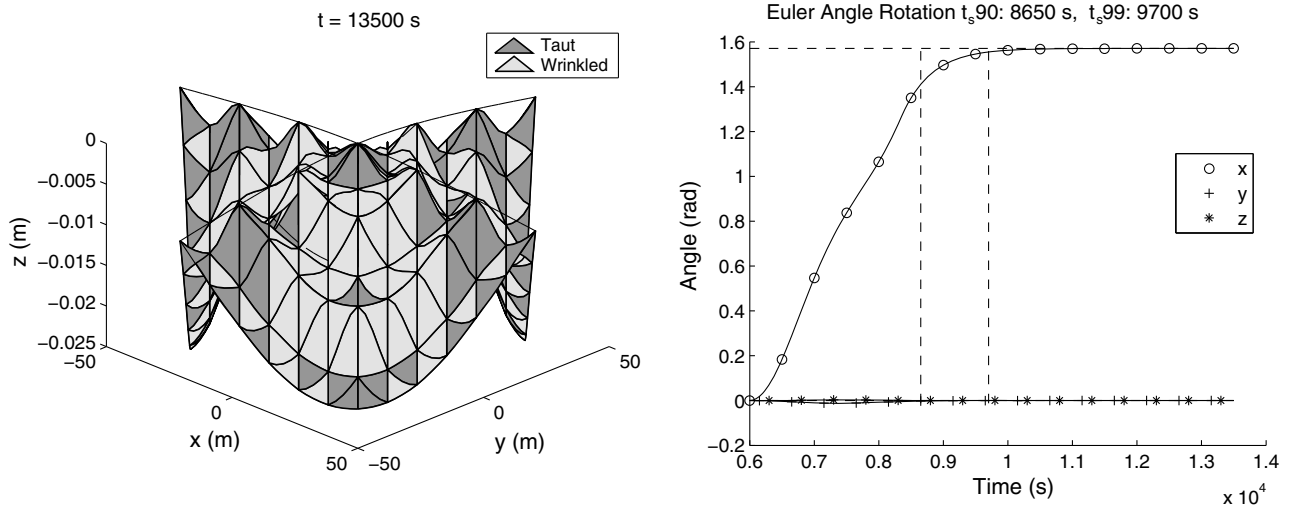

a) Isometric view

b) Sail attitude in euler angle with 90/99% settling time

Fig. 12 Control simulation for $\theta_x = \pi/2$ and $\theta_y = \theta_z = 0$.

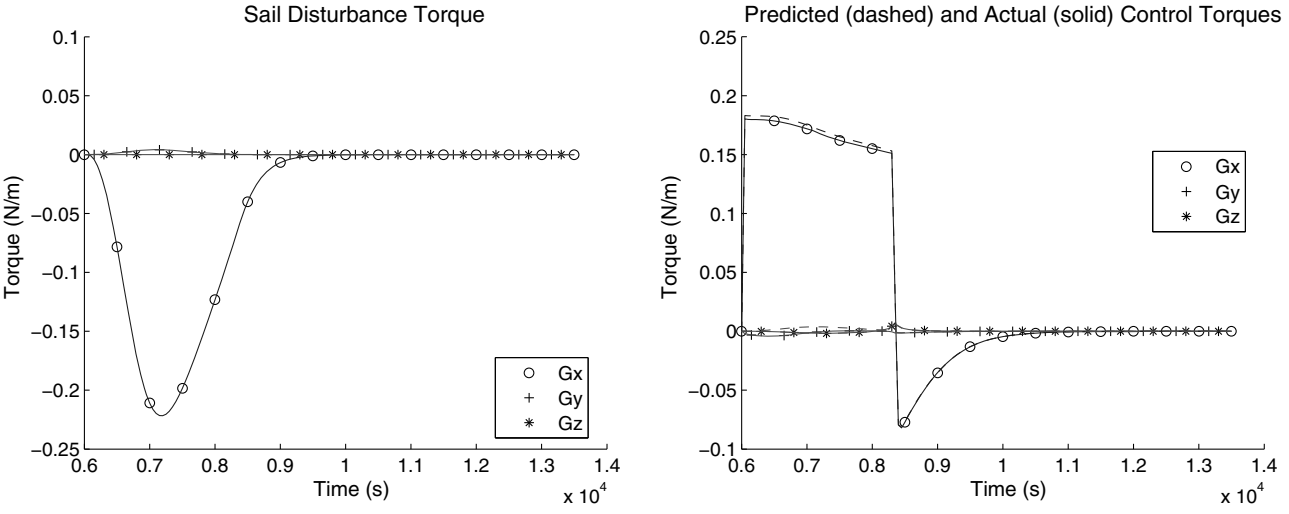

a) Sail disturbance torque

b) Predicted (dashed) and actual (solid) control torques

Fig. 13 Disturbance and control torques during control simulation for $\theta_x = \pi/2$ and $\theta_y = \theta_z = 0$.

to the sun, with the boom sag reaching its minimum and only slightly deviating from the straight boom case assumed by the control allocation algorithm.

Vane angles commanded by the control allocation algorithm are plotted in Fig. 14. It can be seen that, for the most part, the changes to the angles are not too abrupt, with the exceptions being ϕ_2 dropping sharply at around 7000 s and θ_2 and θ_4 wrapping around at π. The wraparound experienced by θ is an expected behavior, and the abrupt change experienced by ϕ_2 occurs at around the same time θ_2 goes from near zero to $-\pi$, which is most likely the main cause. A detailed study into the behavior of the single-vane analytical solution would be needed to mitigate such changes.

An interesting case to consider is the case when the sail is commanded to $\theta_x = \theta_z = \pi/4$: specifically, tuning the proportional gain to allow the Euler angles to settle to 99% of the desired attitude within a reasonable time causes significant overshoot along θ_z, which is deemed undesirable. Increasing the derivative gain to mitigate the overshoot results in significant oscillation in the control torques, which is a highly undesirable behavior. What is shown in Fig. 15 is a result of multiple attempts to tune the gain parameters such that a 99% settling state is reached without significant overshoot and control torque oscillation. The shape of the sail is a reduced catenary billow from the original steady-state simulation but with a caveat. There is a notable difference in displacement between the left and the right sides of the sail. The sail membranes are more perpendicular to the sun vector on the right side than the left side due to the inherent slant in each quadrant, which results in greater force produced on the right side, and hence the greater sail deflection on the right side. The Euler angle plot shown in Fig. 15 indicates that there is a 20% overshoot for θ_z, along with an unimpressive settling time of nearly 5000 s (albeit 90% settling state was reached earlier on). In addition, there is a θ_y undershoot observed here, which is likely due to the disturbance the sail undergoes as it slews to the desired attitude. A dip in attitude for θ_x is also observed around the time θ_z experiences an overshoot, which is the most likely cause of the dip.

The disturbance torque and the control torques are shown in Fig. 16. The disturbance remains biased, acting against the control torque to restore the sail attitude back to the sun-facing direction. One can clearly see the effect of the bias on the control torque: Fig. 16b shows how G_x and G_y are set to nonzero values even after the slew has completed. The plot also shows that the changes in these control torques are not as sudden as the previous simulation, but this is likely attributed to the slower convergence experienced by this particular simulation compared to them. In addition, a small amount of control torque oscillation can be seen between 9000 and 10,000 s, which does damp out but is a cause for concern.

The general trend for the vane angles as seen in Fig. 17 is that moderate changes are observed throughout the first 4000 s, which

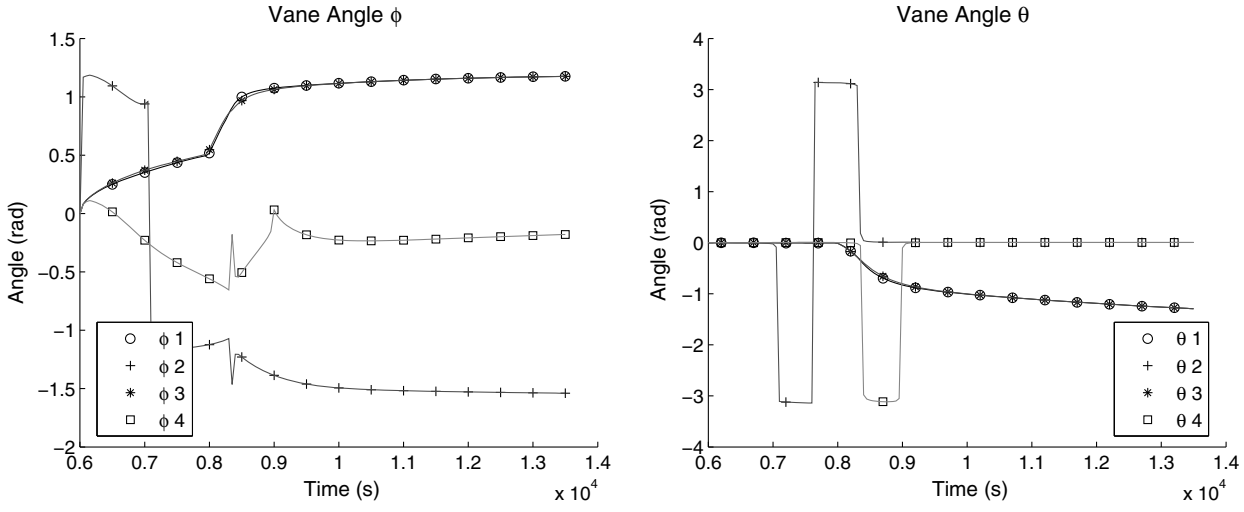

a) Vane angle ϕ **b) Vane angle θ**

Fig. 14 Vane angles during control simulation for $\theta_x = \pi/2$ and $\theta_y = \theta_z = 0$.

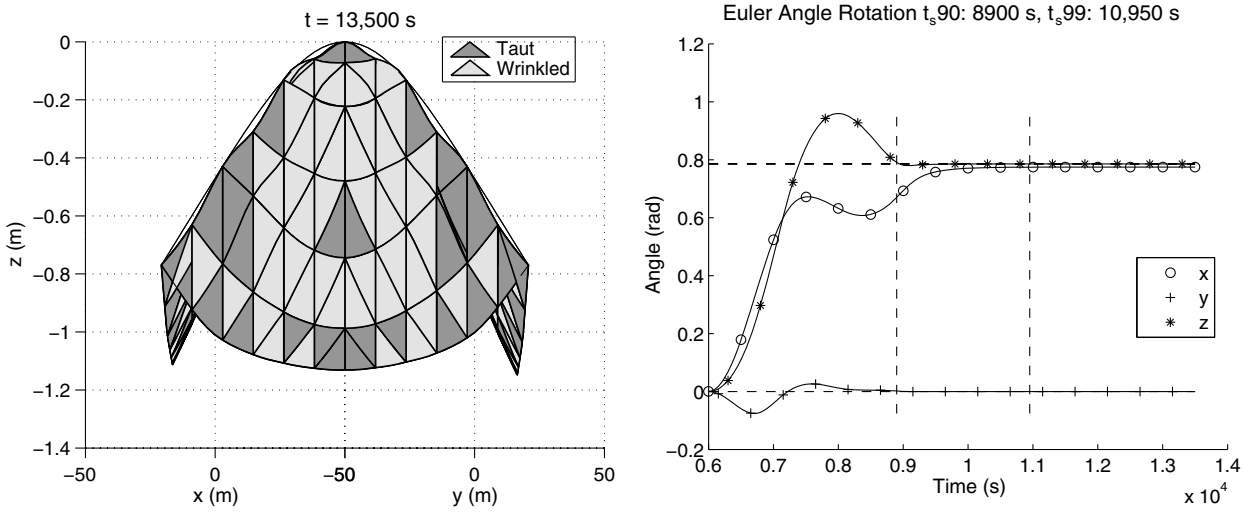

a) Side view **b) Sail attitude in euler angle with 90/99% settling time**

Fig. 15 Control simulation for $\theta_x = \theta_z = \pi/4$ and $\theta_y = 0$.

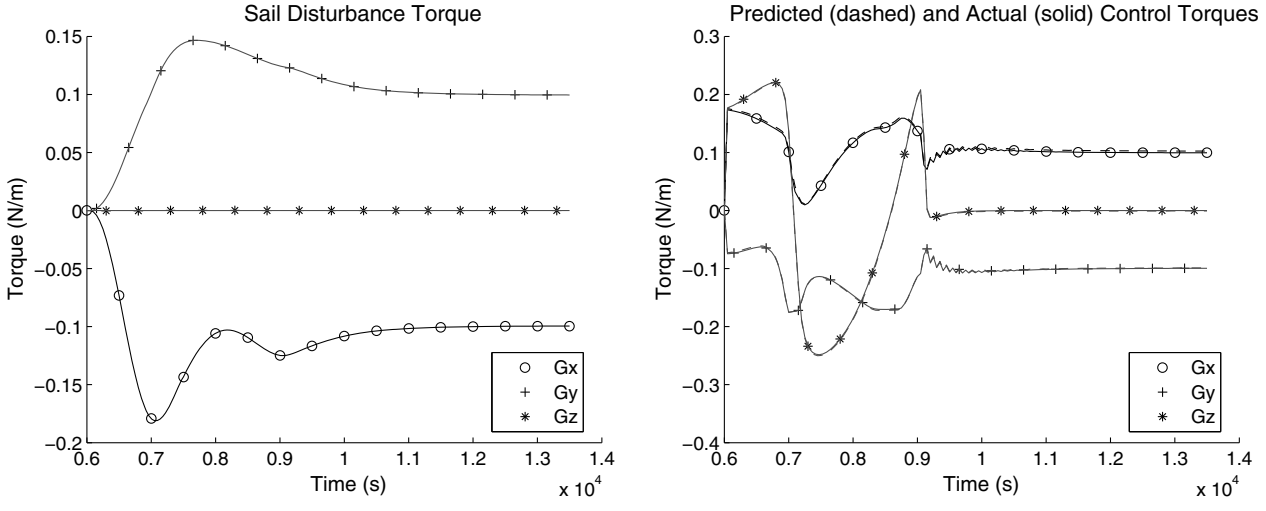

a) Sail disturbance torque **b) Predicted (dashed) and actual (solid) control torques**

Fig. 16 Disturbance and control torques during control simulation for $\theta_x = \theta_z = \pi/4$ and $\theta_y = 0$.

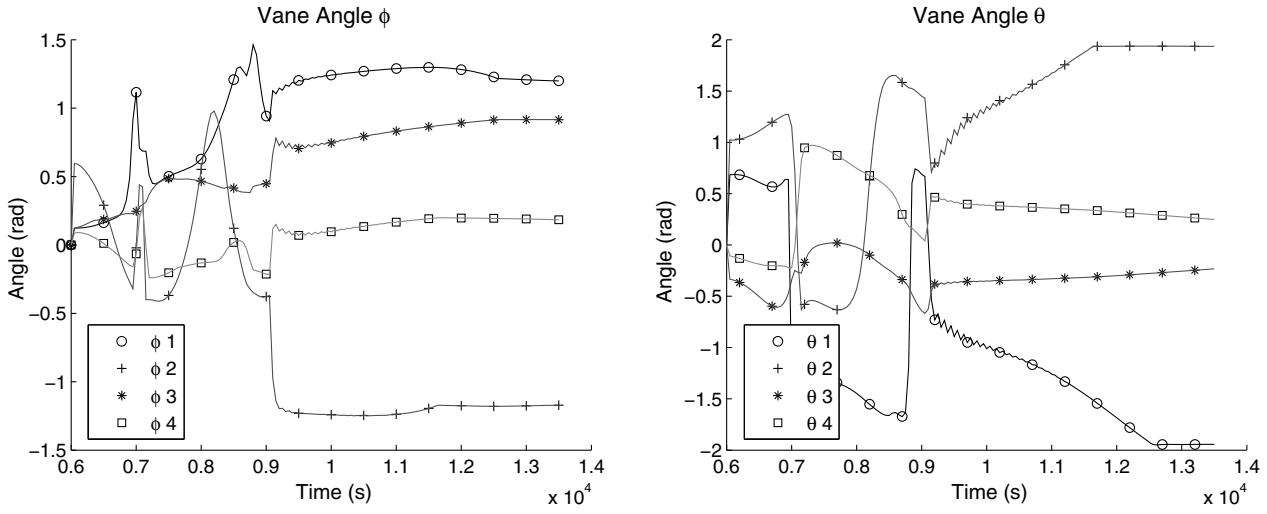

a) Vane angle ϕ **b) Vane angle θ**

Fig. 17 Vane angles during control simulation for $\theta_x = \theta_z = \pi/4$ and $\theta_y = 0$.

then experience a brief oscillation between 9000 to 10,000 s before settling down to a smoother curve for the remainder of the simulation. The behavior of the first 4000 s corresponds to the rapid changes in the control torque. The oscillation is clearly due to the control torque oscillation from Fig. 16b. It is worthwhile to note that the vane angles do not experience the θ wraparound seen in other simulations.

Note that this attitude can also be achieved by a sequentially commanded set of attitudes (first, turn the sail about the z axis by $\pi/4$, and then about the x axis by $\pi/4$); the resulting attitude is equivalent, but it allows two different gains to be used to control each rotation maneuver separately. One such simulation is shown in Fig. 18. To achieve this, the simulation was initially set with $k_p = 1 \times 10^6$ P N $\cdot$ m/rad and $K_d = 2.2 \times 10^2 k_p 1_3$ N $\cdot$ m/rad/s; then, with those control gains, the sail is commanded to the first attitude in the sequence — $\theta_x = \theta_y = 0$, and $\theta_z = \pi/4$. These control gains and the desired attitude are maintained until the 99% settling state is reached: in the case of this particular simulation, this is at 8000 s and denoted by the dotted–dashed line in Fig. 18a.

Once the first sequence attitude is achieved, a new set of control gains is specified: $k_p = 1.5 \times 10^6$ P N $\cdot$ m/rad and $K_d = 9 \times 10^1 k_p 1_3$ N $\cdot$ m/rad/s, with the new desired attitude set as $\theta_x = \pi/4$, $\theta_y = 0$, and $\theta_z = \pi/4$. One can immediately observe its effects from Fig. 18a, where θ_x begins its ascent to the desired value. One can also observe a slight overshoot, no doubt caused by the changing θ_x and the resulting disturbance, but because it is already close to its desired value, it is able to quickly settle back. At the same time, since θ_x is the only angle with large changes, the controller is able to provide appropriate torques to converge to its desired value within a short period of time. The convergence behavior is similar to the second simulation: after the second sequence is commanded, the sail attitude reaches a 90% settling state at around 1000 s, and it takes another 2000 s to converge to the 99% settling state. The combined 99% settling time for the two sequences is 5150 s, which is only 200 s longer than the previous simulation, and it avoids most of the issues associated with it.

Note that, based on what is seen in Fig. 18b, one could argue that the controller behavior of the previous simulation is preferable to this one, which contains several steep jumps from one set of torques to another. Such changes to the control torques result in rapid and sudden changes to the vane angles, as shown in Fig. 19, particularly at around 9000 s when the sail reaches 90% settling state. Once again, this is presumably due to the compensation action for the rapid slewing experienced by the sail, which is necessary to keep the sail pointing in the right direction against the biased sail SRP torques.

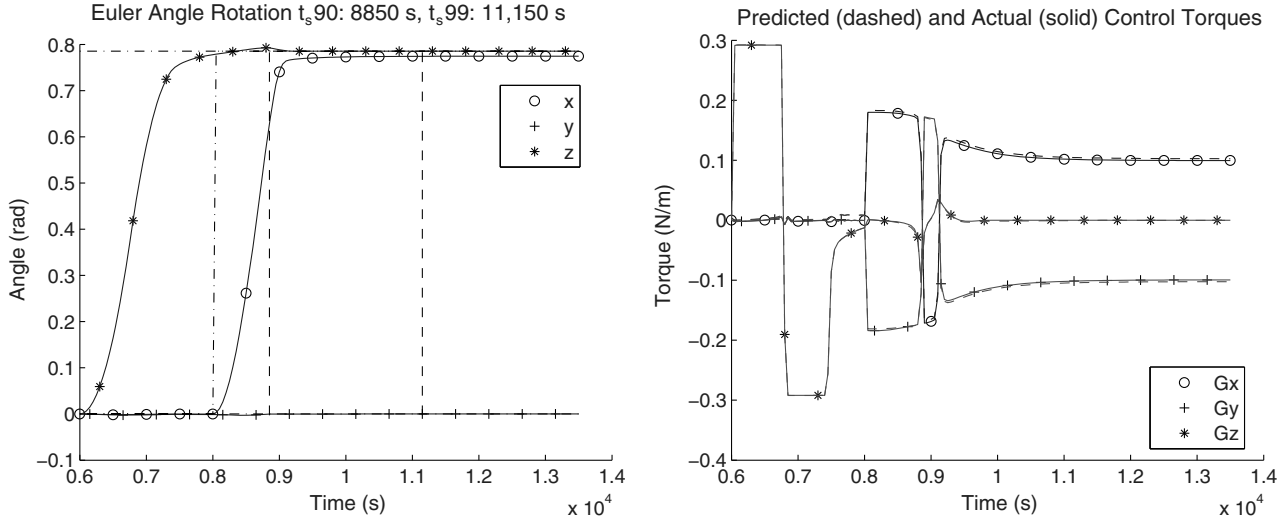

a) Sail attitude in euler angle with 90/99% settling time **b) Predicted (dashed) and actual (solid) control torques**

Fig. 18 Vane angles during control simulation for $\theta_x = \theta_z = \pi/4$ and $\theta_y = 0$, with sequential commands.

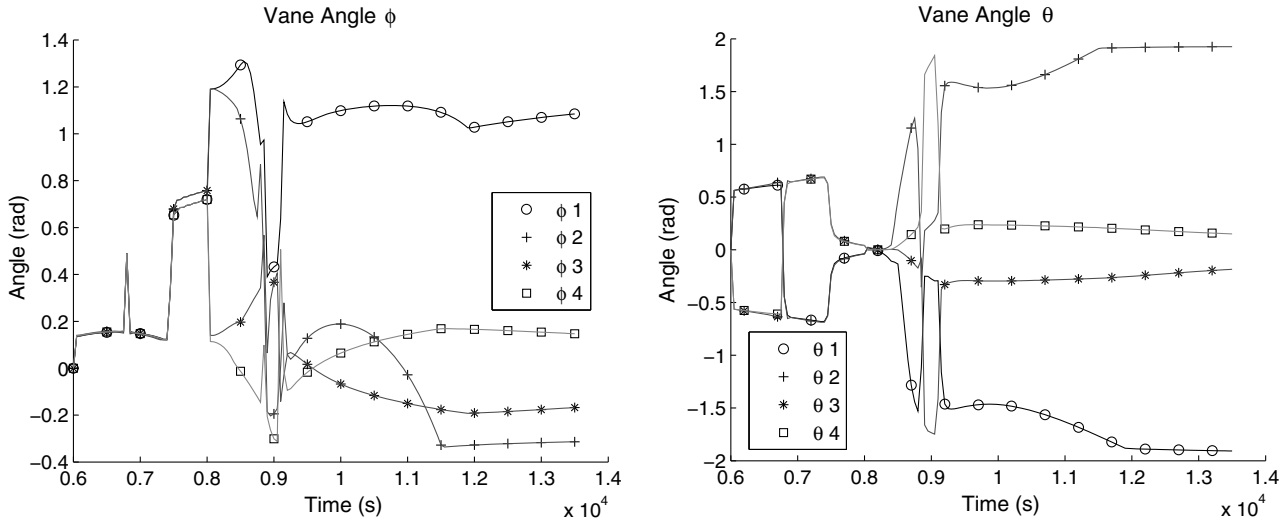

a) Vane angle ϕ **b) Vane angle θ**

Fig. 19 Vane angles during control simulation for $\theta_x = \theta_z = \pi/4$ and $\theta_y = 0$, with sequential commands.

X. Conclusions

This paper presented a structural and attitude control dynamics simulation of a cord-mat solar sail, containing a number of considerations unique to solar sailing. Two unique disturbance factors were added to the FEM model of the solar sail and the unconstrained nonlinear structural dynamics equations describing the model. One is the wrinkling sail membrane model, where the membrane's stress–strain constitutive relationship is modified to portray the changing behavior of the membrane as different forces acted upon it. The other is the sail shadowing model, where shading caused by different portions of the spacecraft is identified based on a parallel projection method. This takes advantage of the specific choice of the FEM element used for this research to determine specific shaded nodes and removes their contributions to the SRP force produced by the sail. The sail model combined with the disturbance factors was used to then verify the capability of the tip-vane attitude actuators and the associated control allocation scheme by using a simple PD control law to command the sail to a number of pointing directions, with the results illustrated in graphs and analyzed. The results are promising, showing that the control scheme is capable of rotating the sail to the desired pointing direction roughly within 2 h.

References

[1] Wie, B., "Solar Sail Attitude Control and Dynamics, Part 1," *Journal of Guidance, Control, and Dynamics*, Vol. 27, No. 4, 2004, pp. 526–535. doi:10.2514/1.11134

[2] Wie, B., "Solar Sail Attitude Control and Dynamics, Part 2," *Journal of Guidance, Control, and Dynamics*, Vol. 27, No. 4, 2004, pp. 536–544. doi:10.2514/1.11134

[3] Polites, M., Kalmanson, J., and Mangus, D., "Solar Sail Attitude Control Using Small Reaction Wheels and Magnetic Torquers," *Journal of Aerospace Engineering*, Vol. 222, No. 1, 2008, pp. 53–62. doi:10.1243/09544100JAERO250

[4] Wie, B., "Thrust Vector Control Analysis and Design for Solar-Sail Spacecraft," *Journal of Spacecraft and Rockets*, Vol. 44, No. 3, 2007, pp. 545–557. doi:10.2514/1.23084

[5] Wie, B., and Murphy, D., "Robust Attitude Control Systems Design for Solar Sails, Part 1: Propellantless Primary ACS," *AIAA Guidance, Navigation, and Control Conference and Exhibit*, AIAA Paper 2004-5010, 2004.

[6] McInnes, C., *Solar Sailing: Technology, Dynamics and Mission Applications*, Springer Praxis, New York, 1999, pp. 76–78, 38–39, 46–51.

[7] Greschik, G., and Mikulas, M., "Design Study of a Square Solar Sail Architecture," *Journal of Spacecraft and Rockets*, Vol. 39, No. 5, 2002, pp. 653–661. doi:10.2514/2.3886

[8] Greschik, G., "The Cord Mat Sail—Concept, Mechanics, and Design Example," *46th AIAA/ASME/ASCE/AHS/ASC Structures, Structural Dynamics and Materials Conference*, AIAA Paper 2005-2049, 2005.

[9] Greschik, G., "A Linear Photonic Thrust Model and Its Application to the L'Garde Solar Sail Surface," *54th AIAA/ASME/ASCE/AHS/ASC Structures, Structural Dynamics, and Materials Conference*, AIAA Paper 2013-1803, 2013.

[10] Macdonald, M., Hughes, G., and McInnes, C., "GeoSail: An Elegant Solar Sail Demonstration Mission," *Journal of Spacecraft and Rockets*, Vol. 44, No. 4, 2007, pp. 784–796. doi:10.2514/1.22867

[11] Derbes, B., and Veal, G., "Team Encounter Solar Sails," *45th AIAA/ASME/ASCE/AHS/ASC Structures, Structural Dynamics, and Materials Conference*, AIAA Paper 2004-1577, 2004.

[12] Murphy, D., Murphey, T., and Gierow, P., "Scalable Solar-Sail Subsystem Design Concept," *Journal of Spacecraft and Rockets*, Vol. 40, No. 4, 2003, pp. 539–547. doi:10.2514/2.3975

[13] Zeiders, G., "Design Rules and Scaling for Solar Sails," *41st AIAA/ASME/SAE/ASEE Joint Propulsion Conference and Exhibit*, AIAA Paper 2005-4553, 2005.

[14] Sleight, D., and Muheim, D., "Parametric Studies of Square Solar Sails Using Finite Element Analysis," *45th AIAA/ASME/ASCE/AHS/ASC Structures, Structural Dynamics, and Materials Conference*, AIAA Paper 2004-1509, 2004.

[15] Choi, M., "Flexible Dynamics and Attitude Control of a Square Solar Sail," Ph.D. Thesis, Univ. of Toronto, Inst. for Aerospace Studies, Toronto, 2014.

[16] Timoshenko, S., and Woinowsky-Krieger, S., *Theory of Plates and Shells*, 2nd ed., McGraw–Hill, New York, 1959, p. 415.

[17] Shampine, L., and Reichelt, M., "The Matlab ODE Suite," *SIAM Journal on Scientific Computing*, Vol. 18, No. 1, 1997, pp. 1–22. doi:10.1137/S1064827594276424

[18] Adler, A. L., and Mikulas, M. M., "Application of a Wrinkled Membrane Finite Element Approach to Advanced Membrane Structures," *AIAA/ASME/ASCE/AHS Structures, Structural Dynamics, and Materials Conference*, AIAA Paper 2001-4646, 2001.

[19] Miyazaki, Y., "Wrinkle/Slack Model and Finite Element Dynamics of Membrane," *International Journal for Numerical Methods in Engineering*, Vol. 66, No. 7, 2005, pp. 1179–1209. doi:10.1002/(ISSN)1097-0207

[20] Akita, T., Nakashino, K., Natori, M., and Park, K., "A Simple Computer Implementation of Membrane Wrinkle Behaviour via a Projection Technique," *International Journal for Numerical Methods in Engineering*, Vol. 71, No. 10, 2007, pp. 1231–1259. doi:10.1002/(ISSN)1097-0207

[21] Lee, E., and Youn, S., "Finite Element Analysis of Wrinkling Membrane Structures with Large Deformations," *Finite Elements in Analysis and Design*, Vol. 42, Nos. 8–9, 2006, pp. 780–791. doi:10.1016/j.finel.2006.01.004

[22] Roddeman, D., Drukker, J., Oomens, C., and Janssen, J., "The Wrinkling of Thin Membranes: Part I—Theory," *Journal of Applied*

Mechanics, Vol. 54, No. 4, 1987, pp. 884–887.
doi:10.1115/1.3173133

[23] Roddeman, D., "Finite-Element Analysis of Wrinkling Membranes," *Communications in Applied Numerical Methods*, Vol. 7, No. 4, 1991, pp. 299–307.
doi:10.1002/(ISSN)1555-2047

[24] Liu, X., Jenkins, C. H., and Schur, W. W., "Large Deflection Analysis of Pneumatic Envelopes Using a Penalty Parameter Modified Material Model," *Finite Elements in Analysis and Design*, Vol. 37, No. 3, 2001, pp. 233–251.
doi:10.1016/S0168-874X(00)00040-8

[25] Jarasjarungkiat, A., Wuchner, R., and Bletzinger, K.-U., "Efficient Sub-Grid Scale Modeling of Membrane Wrinkling by a Projection Method," *Computer Methods in Applied Mechanics and Engineering*, Vol. 198, Nos. 9–12, 2009, pp. 1097–1116.
doi:10.1016/j.cma.2008.11.014

[26] Kang, S., and Im, S., "Finite Element Analysis of Dynamic Response of Wrinkling Membranes," *Computer Methods in Applied Mechanics and Engineering*, Vol. 173, Nos. 1–2, 1999, pp. 227–240.
doi:10.1016/S0045-7825(98)00271-0

[27] Kang, S., and Im, S., "Finite Element Analysis of Wrinkling Membranes," *Journal of Applied Mechanics*, Vol. 64, No. 2, 1997, pp. 263–269.
doi:10.1115/1.2787302

[28] Pimprikar, N., Banerjee, B., Roy, D., Vasu, R., and Reid, S., "New Computational Approaches for Wrinkled and Slack Membranes," *International Journal of Solids and Structures*, Vol. 47, Nos. 18–19, 2010, pp. 2476–2486.
doi:10.1016/j.ijsolstr.2010.05.004

[29] Miller, R., Hedgepeth, J., Weingarten, V., Das, P., and Kahyai, S., "Finite Element Analysis of Partly Wrinkled Membranes," *Computers and Structures*, Vol. 20, Nos. 1–3, 1985, pp. 631–639.
doi:10.1016/0045-7949(85)90111-7

[30] Cormen, T. H., Leiserson, C. E., Rivest, R. L., and Stein, C., *Introduction to Algorithms*, 2nd ed., MIT Press and McGraw–Hill, New York, 2001, pp. 955–956.

[31] Choi, M., and Damaren, C. J., "Control Allocation of Solar Sail Tip Vanes with Two Degrees of Freedom using Elliptical Constraints," *AIAA Guidance, Navigation and Control Conference*, AIAA Paper 2012-5002, 2012.

[32] Wen, J. T., and Kreutz-Delgado, K., "The Attitude Control Problem," *IEEE Transactions on Automatic Control*, Vol. 36, No. 10, 1991, pp. 1148–1162.
doi:10.1109/9.90228

[33] Hughes, P. C., and Skelton, R. E., "Controllability and Observability for Flexible Spacecraft," *Journal of Guidance, Control, and Dynamics*, Vol. 3, No. 5, 1980, pp. 452–459.
doi:10.2514/3.56020

M. Xin
Associate Editor